analytical chemistry

Article

pubs.acs.org/ac

Electrochemically Deposited Pd–Pt and Pd–Au Codeposits on Graphite Electrodes for Electrocatalytic H_2O_2 Reduction

Tharamani Chikka Nagaiah,[†,#] Dominik Schäfer,[†] Wolfgang Schuhmann,*[,†] and Nina Dimcheva*[,†,‡]

[†]Analytische Chemie - Elektroanalytik & Sensorik, Ruhr-University Bochum, Universitätsstr. 150, D-44780 Bochum, Germany

[‡]Department of Physical Chemistry, Plovdiv University, 24, Tsar Assen st., Plovdiv-4000, Bulgaria

Supporting Information

ABSTRACT: Improved electrocatalytic activity and selectivity for the reduction of H_2O_2 were obtained by electrodepositing Pd–Pt and Pd–Au on spectrographic graphite from solutions containing salts of the two metals at varying ratio. The electrocatalytic activity of the resulting binary codeposits for H_2O_2 reduction was evaluated by means of the redox-competition mode of scanning electrochemical microscopy (SECM) and voltammetric methods. In a potential range from 0 to −600 mV (vs. Ag/AgCl/3 M KCl) at pH 7.0 in 0.1 M phosphate citrate buffer, the electrocatalytic activity of both Pd–Pt and Pd–Au codeposits was substantially improved as compared with the identically deposited single metals suggesting an electrocatalytic synergy of the codeposits. Pd–Pt and Pd–Au codeposits were characterized by X-ray diffraction (XRD) analysis and scanning electron microscopy (SEM). Codepositing with Au caused a change of hedgehog-like shaped Pd nanoparticles into cauliflower-like nanoparticles with the particle size decreasing with increasing Au concentration. Codepositing Pd with Pt caused the formation of oblong structures with the size initially increasing with increasing Pt content. However, the particle size decreases with further increase in Pt concentration. The improved electrocatalytic capability for H_2O_2 reduction of the Pd–Pt electrodeposits on graphite was further demonstrated by immobilizing glucose oxidase as a basis for the development of an interference-free amperometric glucose biosensor.

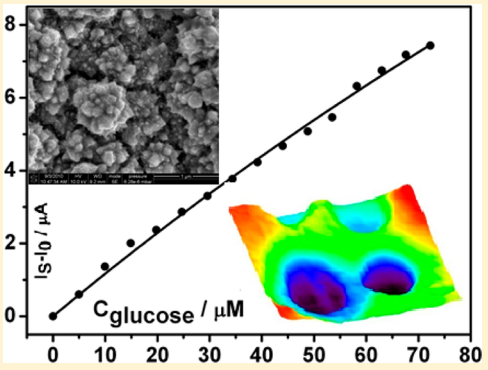

Electrocatalytic activity of platinum group metals is well documented and is extensively studied. Their binary alloys with other transition metals have been found to considerably improve both catalyst selectivity and durability.[1] Pd and Pt are well-known catalyst materials for the electrochemical reduction of H_2O_2;[2,3] however, the catalytic activity of their codeposits was mainly investigated with respect to fuel oxidation at the anode of fuel cells.[4,5] Recently, Pd–Au membranes have been found capable of mediating the direct synthesis of H_2O_2 from O_2 and H_2.[6,7] Earlier, thin layers of Pd–Au sputtered on carbonaceous materials were intensively investigated as H_2O_2 sensors.[8,9] Both electrochemical oxidation as well as reduction of H_2O_2 using Pd–Au modified graphite electrodes exhibited low overpotentials, a linear dynamic range spanning over 4 orders of magnitude and extended electrode stability. Similarly, stable electrodes were obtained using electrochemically codeposited thin Pd–Pt films[10] on porous graphite and proposed as amperometric sensors for H_2O_2 monitoring. The electrodeposition of thin Pd–Au films was further performed on glassy carbon surfaces yielding low-noise, sensitive, and highly reproducible H_2O_2 sensors.[11] However, these sensors were lacking sufficient mechanical stability due to the poor adhesion of the bimetallic codeposits on the glassy carbon surface. Despite the fact that these types of modified electrodes were suggested as potential transducers for amperometric oxidase-based biosensors, all previously described electrode configurations using noble metal codeposits for H_2O_2 detection exhibited noticeable interference to oxygen.

In general, the investigation of the electrocatalytic properties of catalysts toward O_2 and H_2O_2 reduction are performed using cyclic voltammetry, rotating disc electrode, rotating ring disc electrode, and amperometric measurements. In addition, scanning electrochemical microscopy (SECM) has been used to evaluate the local electrocatalytic activity of catalyst surfaces, employing the sample generation/tip collection mode (SG-TC) or the tip generation/sample collection mode (TG-SC).[12] It was demonstrated that improved spatial resolution can be obtained by means of the redox competition mode (RC-SECM), which is a bipotentiostatic experiment in which the tip and the sample compete for the same analyte.[13]

In this contribution, we investigate the catalytic activity of Pd–Pt and Pd–Au electrodeposits on graphite with respect to the reduction of H_2O_2 or O_2 using cyclic voltammetry, amperometry, and rotating disc electrode measurement. RC-SECM studies were additionally carried out to visualize the local catalytic activity and selectivity of Pd–Pt and Pd–Au codeposits toward H_2O_2 and O_2 reduction. The surface morphology and microstructure of the catalyst codeposits

Received: May 26, 2013
Accepted: July 19, 2013

   dx.doi.org/10.1021/ac401317y | *Anal. Chem.* XXXX, XXX, XXX–XXX

were studied using scanning electron microscopy (SEM) and X-ray diffraction (XRD). The obtained results allow for the evaluation of the impact of the catalyst loading on the electrocatalytic behavior toward H_2O_2 reduction and possible applications of the most active electrocatalyst in the glucose biosensor.

EXPERIMENTAL SECTION

Materials. Rods of spectroscopic graphite RW0 (Ringsdorf, Germany) with different diameters (3 mm, 5 mm or 12 mm) were used as electrode materials. $PdCl_2$, H_2PtCl_6, or $HAuCl_4$ were dissolved in 0.1 M HCl to obtain 2% solutions of the metal salts. The $PdCl_2$ solution was then mixed with either of the two other solutions in different proportions so that the resulting deposition solution contained Pd and Pt in the ratios (wt/wt %) of 90:10, 70:30, and 50:50 designated as $Pd_{90}Pt_{10}$, $Pd_{70}Pt_{30}$, and $Pd_{50}Pt_{50}$, respectively. Similarly, mixtures of Pd and Au were prepared designated as $Pd_{90}Au_{10}$, $Pd_{70}Au_{30}$, and $Pd_{50}Au_{50}$.

Glucose oxidase (GOx; E.C. 1.1.3.4) from *Aspergillus niger* (Fluka, Germany) had an activity of 198 U mg^{-1}. D-Glucose monohydrate (Sigma-Aldrich, Germany) was allowed to mutarotate at a concentration of 2 mM in 0.1 M phosphate buffer (PCB), pH 7.0 for 24 h before use. H_2O_2 and salts for the preparation of buffer solutions, namely, $K_2HPO_4{\cdot}12H_2O$, citric acid, KOH, and H_3PO_4 were of analytical grade. All solutions were prepared with double distilled water.

Electrode Preparation. Graphite rods (Ø, 5 and 3 mm) were connected with current leads and fitted into a Teflon insulation. Before use, all electrodes were polished on fine emery paper with decreasing particle size (P800, P1500, P2000), washed with double distilled water, and then sonicated for 3 min in double distilled water, again thoroughly rinsed with water and dried in air. The metal codeposits were obtained by applying a constant potential of $E_r^{deposit}$ = +50 mV vs NHE (= −155 mV vs Ag/AgCl/3 M KCl) for 3 s from a solution containing either of the above binary solutions mixed in different ratios or $PdCl_2$, H_2PtCl_6, and $HAuCl_4$ alone. Between measurements, the metal-modified graphite electrodes were kept in double distilled water to avoid surface contaminations.

Enzyme electrodes were prepared as reported previously.[10b,d,e] In brief, the modified graphite electrode was dipped in glucose oxidase solution (5 mg mL^{-1} in 0.1 M PCB, pH 7.0), and the enzyme was allowed to adsorb for 1 h. Then, the surface was kept in air for 15 min covered with a 10 μL drop of 5% gelatin suspension mixed with the enzyme solution in the ratio 1:1 (v/v). The enzyme layer was dried in Ar and then used for experiments. After measurements, the enzyme electrodes were carefully rinsed with double distilled water, dried, covered with a small vial, and kept refrigerated for up to 1 week.

SEM, AFM, and XRD Studies. Surface morphology, composition, and microstructure of the Pd−Pt and Pd−Au codeposits on graphite electrodes were evaluated by means of a FEI ESEM Dual Beam Quanta 3D FEG scanning electron microscope with an energy diffraction X-ray analysis (EDAX) system (Genesis XM2i). The X-ray diffraction patterns were recorded in the 2θ range from 10 to 70° (step width of 0.0308) with a Panalytical MPD diffractometer using Cu Kα radiation (λ = 1.5418 Å) at 45 kV and 40 mA, 0.58 divergent and antiscatter slits, a 0.2 mm high receiving slit, incident and diffracted beam 0.04 rad soller slits, and a secondary graphite monochromator.

Atomic force microscopy (AFM) was performed using a NanoWizard 3 AFM controlled by a JPK SPM Control Station III (JPK Instruments, Germany) mounted on a vibration damping table Vario Control Micro 40 (Halcyonics, Germany). Cantilevers were made of doped single crystal Si (type ACTA, Applied Nanostructures, USA), with a tip-radius of <10 nm, a spring constant of ∼40 N m^{-1}, and an Al coating on the reflecting side. All images were acquired ex situ using tapping mode under ambient laboratory conditions with a tip velocity of 5 μm s^{-1}.

Sample Preparation for RC-SECM Studies. For SECM studies, graphite rods with 12 mm diameter were sliced to ∼3−4 mm thick discs which were glued to glassy carbon plates with a conductive paste containing colloidal silver. Before use, they were carefully mirror polished. Different composition of Pd−Pt and Pd−Au catalyst spots (Ø ∼ 300−500 μm) were deposited onto graphite discs using a droplet cell[14,15] and the above-mentioned bath compositions. On each disc, 4 catalyst spots were deposited, a pure Pd deposit together with spots with decreasing Pd content replaced by increasing concentrations of either Pt or Au, respectively. The droplet cell consists of a small borosilicate glass capillary (D = 2.5 mm; wall thickness: 0.25 mm, Hilgenberg, Germany), which was pulled to a diameter of about 100−300 μm. A Pt wire served as counter electrode (CE), and a Ag/AgCl/3 M KCl/Agar gel was reference electrode (RE). The droplet cell was positioned directly above the graphite discs assembled on a GC plate, which was used as working electrode (Scheme S1, Supporting Information).

Electrochemical Measurements. The electrocatalytic activity of the Pd−Pt and Pd−Au modified graphite electrodes toward H_2O_2 reduction was determined by cyclic voltammetry (CV) or hydrodynamic linear sweep voltammetry (LSV) using a rotating disc electrode (RDE) with a potentiostat/galvanostat (Autolab PGSTAT12, Ecochemie, The Netherlands) in combination with an analytical rotator (model CTV101; Radiometer, France). A single compartment three-electrode cell was used with a Ag/AgCl/3 M KCl electrode as reference electrode (RE), a Pt wire as counter electrode (CE), either the Pd−Pt or Pd−Au modified graphite electrode as working electrode (WE), and 0.1 M PCB, pH 7.0 as electrolyte solution. LSV measurements (RDE) were recorded in the potential region from +0.6 to −0.5 V with rotation speeds of 200, 350, 500, 750, 1000, and 1200 rpm at a scan rate of 50 mV s^{-1}.

Sensitivity, linear dynamic range, and detection limit for the quantification of H_2O_2 and glucose were evaluated using constant-potential amperometry at 0 V (vs Ag/AgCl/3 M KCl) in 0.1 M PCB, pH 7.0. After establishing the background current, aliquots of 0.01 M H_2O_2 stock solution were added and the current response was recorded. Prior to and during measurements, the solution was purged with Ar in order to remove dissolved O_2. The enzyme electrode was examined similarly by adding aliquots of a 2 mM glucose stock solution. To ensure the flow of oxygen necessary for the enzymatically catalyzed reaction to take place, the electrode was kept close to the boundary of the buffer with air. All amperometric measurements were performed with a portable electrochemical workstation (PalmSens, The Netherlands).

RC-SECM Studies. For SECM measurements, a SECM (Sensolytics, Germany) with the option HighRes was used, and the measurements were carried out using a bipotentiostat (PG 100, Jaissle, Germany). To avoid background current shift caused by uncompensated tilt angles between the scanning plane of the SECM tip and the sample, a software-based

dx.doi.org/10.1021/ac401317y | *Anal. Chem.* XXXX, XXX, XXX−XXX

automatic tilt correction procedure was used. Measurements were carried out in 0.1 M PCB, pH 7.0. A Pt (Goodfellow, Germany) microelectrode (Ø, 25 mm) with a glass-to-metal ratio (RG) of 4.0 was used as SECM tip and was fabricated as described previously.[16] The SECM cell consisted of four electrodes with the sample being either the Pd−Pt or Pd−Au modified graphite rod as working electrode 1 (WE 1), the SECM tip as working electrode 2 (WE 2), a Ag/AgCl/3 M KCl as reference electrode (RE), and a Pt foil as counter electrode (CE), respectively.

Before measurement, three *z*-approach curves were recorded in 0.1 M PCB (pH 7.0) at three *x*,*y*-coordinates of the chosen scan area. The tip potential was kept at −550 mV in order to invoke oxygen reduction while the tip approached the sample surface. In close proximity to the surface, a decrease of the oxygen reduction current at the SECM tip was observed (negative feedback effect). The approach is automatically stopped at a predefined decrease in current response, and the SECM software determines a plane containing the *x*,*y*,*z*-coordinates of the points of closest approach. During scanning, the tip is following this plane, thus keeping the distance between the SECM tip and the plane of the sample surface constant. Due to this automatic tilt correction, the SECM tip could be positioned in comparably close proximity to the sample (10−18 μm) without a substantial risk of tip crash.

RC-SECM[17] was employed to measure the electrocatalytic activity and selectivity of the catalyst toward H_2O_2 reduction. SECM scans were performed with an *x*- and *y*-increment of 50 μm and a tip-to-sample distance of 10 μm. At each point of the predefined *x*,*y*-grid, a pulse potential profile was applied to the tip which consists of six potential steps (Scheme 1) starting with a resting potential of +250 mV (P1) for 500 ms. At this potential, no redox processes at the microelectrode take place and restoration of equilibrium occurs. Then, the potential at the SECM tip is set to +1200 mV for 200 ms (P2; "injection potential") for oxidizing H_2O under formation of O_2, followed by a potential of −550 mV for 500 ms (P3) to invoke oxygen reduction. During the application of P3, the SECM tip and the catalyst modified sample compete for the available O_2 in the gap between tip and sample. The current at the SECM tip during P3 thus reflects the local activity of the underlying sample for the oxygen reduction reaction (ORR). Next, the potentials P1 and P2 are repeated, designated as P4 and P5, followed by P6 at +600 mV for 200 ms, at which H_2O_2, if generated at the sample, is oxidized at the tip. The sample was permanently polarized at −550 mV.

Scheme 1. Schematic Representation of the Reactions Taking Place in the Gap between the Tip and Sample at the Different Potentials Applied Sequentially in the Shown Potential Pulse Profiles at Each Grid Point of the SECM Scan

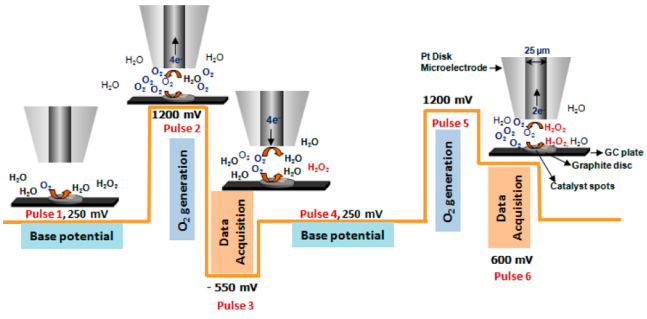

The predetermined sample area was scanned in a "comb-like" mode. The forward line scan in the *x*-direction was slow enough to avoid convection effects, while the backward scan was fast and without data acquisition. Data treatment was performed using the software MIRA (Microscopic Image Rapid Analysis; G. Wittstock, Germany)[18] and OriginPro 7.5 (Microcal, USA). All SECM images were processed with background current subtraction.

RESULTS AND DISCUSSION

Surface Morphology and Microstructure. SEM studies indicated remarkable changes in both the size and shape of the particles upon changing the composition of Pd−Pt and Pd−Au codeposits formed during electrodeposition. Pure Pd deposits show spherically shaped particles covered with needle-like deposits organized in layers (Figure S1A, Supporting Information). The codeposition of Au with Pd causes a change of the particle shape from hedgehog-like to cauliflower-like. Upon increasing the percentage of Au in the electrodeposition bath, the average particle size decreases (Figure S1A-D, Supporting Information) and the particle size distribution becomes less inhomogeneous. Codeposition of Pt with Pd (Figure S2, Supporting Information) causes a change in the particle shape to a spherical/oval shape. Similar to the Pd−Au codeposits, an increased percentage of Pt in the electrodeposition bath leads to a decrease in particle size. Pure Pt particles show a smaller particle size as compared with pure Pd particles. The codeposits form a nonhomogeneous surface with a large number of defects probably caused by evolution of H_2 gas during metal deposition. The layered structure of the codeposits suggests a complex mechanism of the electrodeposition process most likely proceeding via an initial nucleation followed by a progressive growth of particles. No partition into two distinct metal phases can be seen in the SEM images of the codeposits suggesting the formation alloys.

EDX was performed to evaluate the metal ratio in the codeposits. The composition of the Pd−Pt and the Pd−Au codeposits does not reflect the concentration ratio of metal salts in the deposition solution (Table S1 and Figure S3a−d, Supporting Information). Obviously, Pd is predominantly deposited, and hence, the ratio of the metals in the codeposits deviates more from the ratio in the deposition solution at higher relative concentrations of Pt or Au.

XRD measurements of Pd−Pt and Pd−Au codeposits with different Pd−Pt and Pd−Au weight ratios in the deposition solution were carried out (Figure S4A,B, Supporting Information) and compared with those of the pure Pd, Au, and Pt deposits. The peaks at 2θ values of 39.8, 46.5, and 67.8 are characteristics of fcc crystalline Pt (JCPDS 04-0802) corresponding to plane (111), (200), and (220) facets, respectively. Similarly, Pd (JCPDS 04-1043) and Au (JCPDS 04-0784) correspond to plane (111), (200), and (220) facets and exhibit 2θ values of 40.11, 46.65, and 68.12 and 38.18, 44.39, and 64.57, respectively. The pure Pd, Pt, and Au deposits have a single-phase disordered structure. However, the diffraction peaks of Pd−Pt (inset, Figure S4A, Supporting Information) deposits are shifted slightly to higher 2θ values. Similarly, the diffraction peaks of Pd−Au (inset, Figure S3B, Supporting Information) deposits are shifted slightly to lower 2θ values. The lattice expansion caused by the incorporation of Pt or Au atoms into the Pd fcc structure[19] is indicating alloy

dx.doi.org/10.1021/ac401317y | Anal. Chem. XXXX, XXX, XXX−XXX

formation (Figure S4A,B (inset), Supporting Information). With increasing content of Pt or Au the, diffraction peaks arising from Pd−Pt and Pd−Au catalysts shift further to even lower 2θ values indicating a progressive incorporation of Pt or Au. Full peak width at half-maximum (fwhm) calculated from the broadening of the (220) peak changes from 0.376 for Pd and 0.58 for $Pd_{90}Pt_{10}$ to 0.73 for $Pd_{70}Pt_{30}$ and 0.96 for $Pd_{50}Pt_{50}$. Similarly, the codeposition of Au and Pd varied with values of 0.457, 0.84, and 1.126 for $Pd_{90}Au_{10}$, $Pd_{70}Au_{30}$, and $Pd_{50}Au_{50}$, respectively. Obviously, the crystallite size calculated using the Scherrer equation[20] decreases with increasing Pt and Au content in Pd−Pt and Pd−Au codeposits. These results are in good agreement with the corresponding SEM images. The peak at 42.3, 44.4, and 54.5 corresponds to graphitic carbon (JCPDS 41-1487).

The surface topography of the Pd, Pd−Au, and Pd−Pt codeposits was further investigated by means of AFM (Figure S5, Supporting Information). AFM images are consistent with the SEM images and provide more detailed information about the substructure of the codeposits. AFM images show a compact dendritic structure for Pd which changes to smaller cauliflower-like particles upon codeposition with Au or Pt with a uniform size distribution. Despite the morphological changes, the root-mean-square roughness remained between 70 and 300 nm for all samples. The corresponding height profiles reveal that the defect sites display small crevices ranging from 1 to 1.5 μm depth (Pd). However, the depth decreases after codeposition of Au (150−200 nm) and Pt (70−90 nm), suggesting that inhomogeneity of the surface decreases upon codeposition of either of the two metals.

Electrocatalytic Reduction of H_2O_2. Catalytic activities of electrodeposited Pd, Pt, and Au on graphite electrode for the electrochemical reduction of H_2O_2 were evaluated using voltammetric methods (Figure S6, Supporting Information). The reduction of H_2O_2 at both the Pt and Pd modified surfaces shows an onset at a potential of about 0.2 V and reaches a limiting current at potentials below 0 V, while the Au electrodeposits were found to be catalytically inert (not shown). Electrodeposited Pd−Pt and Pd−Au particles with different metal ratios in the codeposits showed similar onset potentials for H_2O_2 reduction (Figure S7, Supporting Information). Obviously, differences in the activity for the electrocatalytic H_2O_2 reduction are dependent on the nature and the amount of the second component in the binary deposits. Increasing the concentration of Pt in Pd−Pt deposits is causing an enhanced response to H_2O_2 reduction (Figure 1A), while increasing the Au concentration in Pd−Au codeposits decreases H_2O_2 reduction (Figure 1B).

Taking into account the changes in morphology and the results for electrocatalytic H_2O_2 reduction activity, an optimal codeposit composition for Pd−Au and Pd−Pt can be obtained resulting in an enhanced H_2O_2 reduction. Amounts of the electrodeposited Pd, Pt, Pd−Au, and Pd−Pt and current response to 10 mM H_2O_2 estimated as the differences with the background current at either 0 mV or the lowest examined potential −400 mV are summarized in Table S2 (Supporting Information).

Visualization of Local Catalytic Activity by Means of SECM. To visualize the local catalytic activity and selectivity toward O_2 reduction and H_2O_2 production, SECM in a sequence of redox-competition mode and generator-collector mode was applied allowing for the simultaneous detection of local O_2 consumption and H_2O_2 production during oxygen

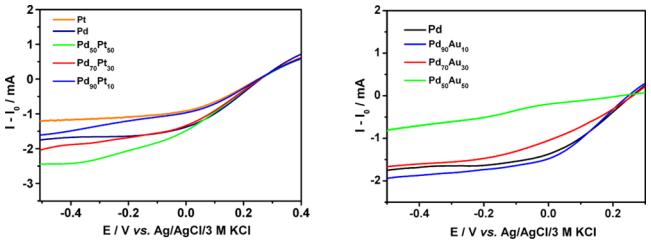

Figure 1. Linear sweep voltammograms (background subtracted current) of (A) Pd−Pt and (B) Pd−Au electrodeposits on graphite electrodes in 10 mM H_2O_2, 0.1 M phosphate buffer, pH 7.0; RE: Ag/AgCl/3 M KCl; CE: Pt foil; rotation rate of 1200 rpm at a scan rate of 50 mV s^{-1}.

reduction at the Pd−Pt or Pd−Au codeposits. Pd−Pt and Pd−Au codeposits with varying relative concentrations of Pd, Pt, and Au were locally deposited using a droplet cell on a 12 mm diameter polished graphite disc (see Scheme S1, Supporting Information). Optical images of the obtained codeposit spots are shown in Figure 2A. The sample potential (E_s) applied to the graphite disc was set to −50, −200, −350, and −550 mV in subsequent experiments.

At each *x*-,*y*-position of the predefined scanned grid, a potential pulse profile as shown in Scheme 1 was applied to the SECM tip. Scheme 1 additionally shows the reactions taking place at the tip at the different applied potentials of the potential pulse sequence. A series of two SECM images are obtained at each *x*-,*y*-position allowing one to select images at a predefined time after the potential application. Figure 2B shows RC-SECM images at decreasing sample potential visualizing the activity of the different codeposits for the oxygen reduction reaction. The left column displays the response of Pd−Pt codeposits with compositions as shown in Figure 2A (left) while the right column displays the response of Pd−Au codeposits with compositions as shown in Figure 2A (right). The images are displayed as an overlay of a 3D representation and a false color scale for the oxygen reduction current at the tip. The 3D representation refers to the current scale of the axes and is the same for all images while the color scheme is spread between the minimum and maximum current in each individual SECM image. As expected, the catalytic activity for oxygen reduction is increasing with decreasing sample potentials; however, distinct differences in the activity are evident for the different codeposit compositions. Interestingly, the electrocatalytic activity for oxygen reduction is improved at all sample potentials by adding 10% of either Pt or Au to Pd. In the case of Pd−Pt codeposits increasing, the Pt content above 10% decreases the oxygen reduction activity. In the case of the Pd−Pt codeposits, compositions with 50/50 and 70/30 are showing a comparatively small oxygen reduction activity at all sample potentials. This effect is less pronounced for the Pd−Au codeposits. At a sample potential of −50 mV, codeposits with Pd−Au of 90/10 and 70/30 exhibit increased oxygen reduction activity. However, Pd−Au 50/50 codeposits are less active than pure Pd deposits. With a decrease in the sample potential to −350 and −550 mV, the electrocatalytic activity for all Pd−Au codeposits becomes similar suggesting that the supply of oxygen within the gap between tip and sample becomes rate limiting.

The second potential pulse sequence as shown in Scheme 1 is establishing a sample generation/tip collection configuration in which H_2O_2 generated at the sample is detected at the tip.

dx.doi.org/10.1021/ac401317y | *Anal. Chem.* XXXX, XXX, XXX−XXX

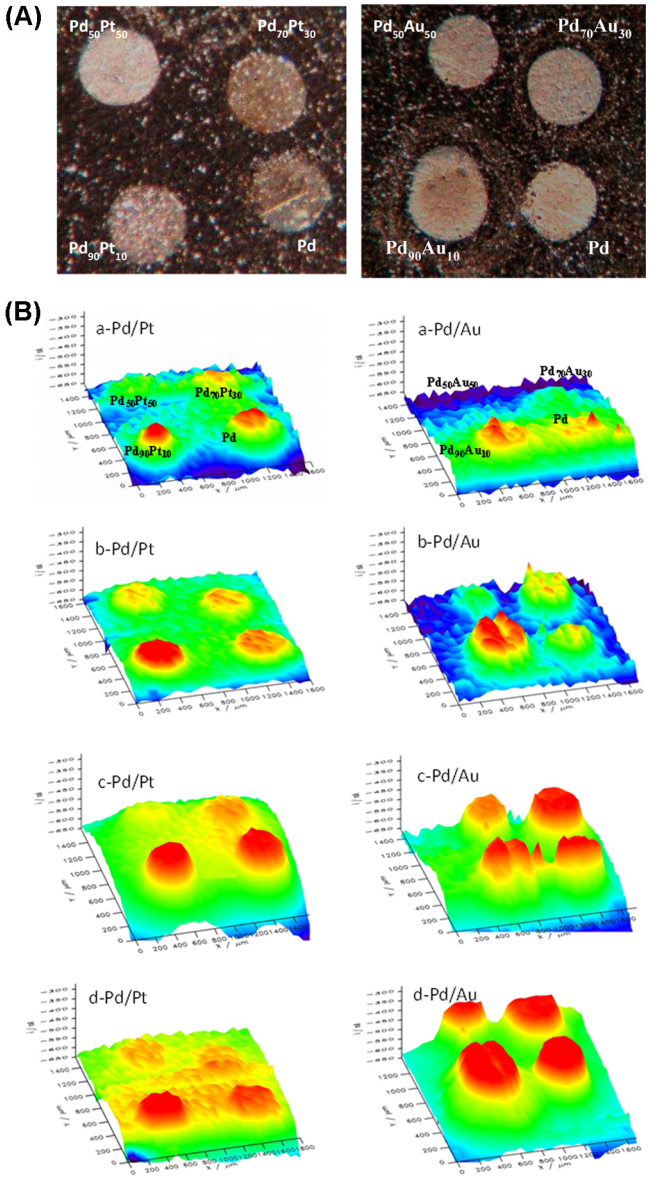

Figure 2. (A) Photograph of the Pd–Pt and Pd–Au spots electrodeposited on a graphite disc with different Pd, Pt, and Au ratios using the droplet cell. (B) Corresponding 3D-SECM images of the electrocatalytic reduction of O_2 over Pd–Pt (left) and Pd–Au codeposits (right) in 0.1 M phosphate buffer, pH 7.0, at different applied sample potentials: −50 mV (a); −200 mV (b); −350 mV (c); −550 mV (d) (vs Ag/AgCl/3 M KCl; pulse 3 in Scheme 1, data taken after 396 ms after applying −550 mV at the SECM tip).

The corresponding SECM images at sample potentials of −350 and −550 mV are shown in Figure S8, Supporting Information. Surprisingly, SECM images show a negative relative tip current obviously resulting from the fact that above the catalyst spots a depletion of H_2O_2 occurs. At the applied sample potentials, reduction of O_2 to H_2O_2 takes place at the surrounding nonmodified graphite surface. Since the electrocatalytic activity of graphite for further reduction of H_2O_2 to H_2O is low, the SECM tip detects a comparably high amount of H_2O_2 generated at the graphite surface. Obviously, at all codeposit spots, the reduction of O_2 is much more pronounced and the reaction proceeds predominantly via a $4e^-$ transfer reaction directly to water. Moreover, any primarily generated H_2O_2 may be readsorbed at the codeposit surface and either further reduced to water or disproportionated to oxygen and water. Due to this, a substantially decreased amount of H_2O_2 becomes available at the SECM tip explaining the current decrease at the tip once it is positioned above either of the codeposits. As a matter of fact, if the catalyst spot produces more H_2O_2 than graphite, the resulting tip current is positive. For better comparability, the generator/collector mode SECM images were inverted (Figure 3) and displayed in a 3D representation overlaid with a false color code for the current. The deeper the blue color, the smaller is the H_2O_2 oxidation current.

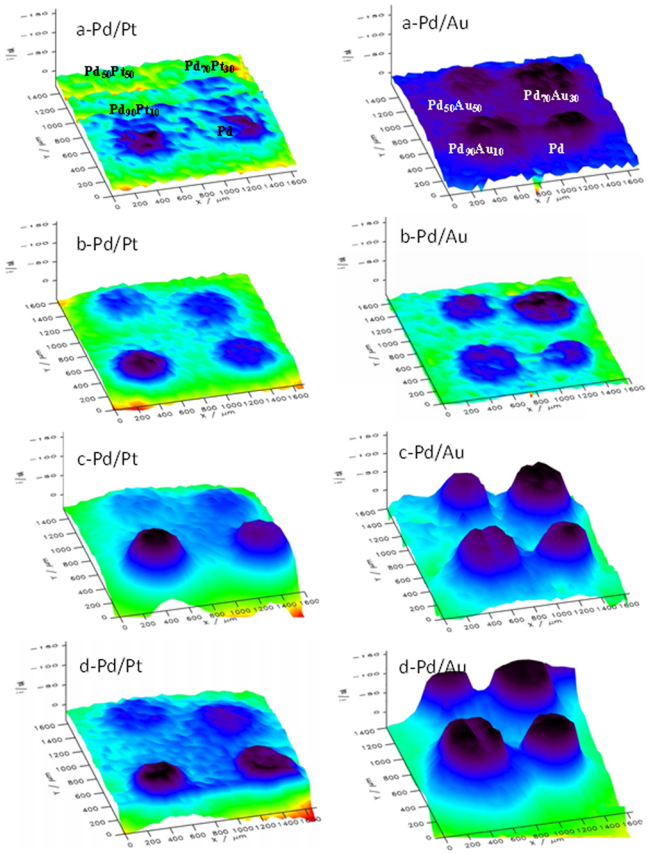

Figure 3. SECM images displaying the inverted tip currents of H_2O_2 oxidation over Pd–Pt (left) and Pd–Au (right) codeposit spots in 0.1 M phosphate buffer, pH = 7.0, at sample potentials of (a) −50 mV, (b) −200 mV, (c) −350 mV, and (d) −550 mV (vs Ag/AgCl/3 M KCl; pulse 6 in Scheme 1, data taken after 396 ms after applying +600 mV at the SECM tip).

All Pd–Au catalyst spots shows a decreased H_2O_2 oxidation current at E_s of −550 and −350 mV (Figure 3, d-Pd–Au and c-Pd–Au) suggesting that the amount of H_2O_2 in the gap between tip and sample is small due to the complete reduction of O_2 to H_2O. This is in agreement with the SECM images displaying O_2 reduction (Figure 2B, d-Pd–Au and c-Pd–Au). In the case of Pd–Pt codeposits, $Pd_{90}Pt_{10}$ shows the lowest H_2O_2 oxidation current. An increasing amount of Pt in the codeposits decreases the oxygen reduction activity on one hand (as shown in Figure 2B) and increases the H_2O_2 oxidation current on the other hand due to an obviously incomplete reduction of O_2. At E_s of −200 and −50 mV, both Pd–Pt and Pd–Au codeposits show an increase in the H_2O_2 oxidation current. Comparing Figure 2B and 3 suggests that at higher sample potentials and increasing amount of both Pt and Au in

dx.doi.org/10.1021/ac401317y | Anal. Chem. XXXX, XXX, XXX–XXX

the codeposits the ORR activity decreases whereas H_2O_2 oxidation increases. SECM line scans displaying the absolute difference in reduction current at the tip over the active spots were plotted for various sample potentials (Figure S9, Supporting Information). The ORR activity of Pd−Pt codeposits shows the order: $Pd_{90}Pt_{10}$> $Pd_{70}Pt_{30}$ > Pd >$Pd_{50}Pt_{50}$. While the reverse trend was observed for H_2O_2 oxidation: $Pd_{50}Pt_{50}$ > $Pd_{70}Pt_{30}$ > Pd > $Pd_{90}Pt_{10}$. A similar trend was observed for the Pd−Au codeposits.

Application in of Pd−Au and Pd−Pt Codeposits as Catalytically Active Sufaces for Biosensors. The small H_2O_2 oxidation current especially for $Pd_{90}Pt_{10}$, $Pd_{90}Au_{10}$, and $Pd_{70}Au_{30}$ codeposits at low sample potential are the basis for potential application in H_2O_2 sensors and, in combination with oxidases, in related biosensors.

A $Pd_{70}Pt_{30}$ modified graphite electrode was tested as H_2O_2 sensor using constant potential amperometry at potentials between −50 and 50 mV (vs. Ag/AgCl/3 M KCl). Optimal current response was obtained at an applied potential of 0 mV, and corresponding H_2O_2 calibration curves for a freshly prepared $Pd_{70}Pt_{30}$ modified graphite electrode and for an electrode used for more than 1 month are shown in Figure 4.

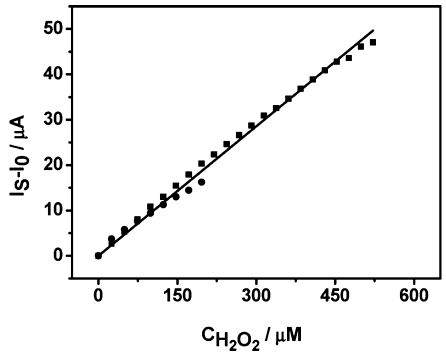

Figure 4. Background subtracted current as a function of H_2O_2 concentration for a freshly prepared (squares) and aged (closed circles) electrode ($Pd_{70}Pt_{30}$/graphite). Linear regression equation: $Y = (0.1021 \pm 0.0011\ \mu A\ \mu M^{-1})X$; $r^2 = 0.999$.

The freshly prepared electrode demonstrates better sensitivity and a substantially extended linear dynamic range (up to 500 μM) as compared to the aged one (up to 100 μM). However, in the linear range, the sensitivity of both electrodes is nearly identical (102 nA μM^{-1}). The sensitivity and the wide linear range provide an excellent basis for the development of amperometric enzyme biosensors. As a model enzyme, glucose oxidase was chosen and immobilized on the surface of a $Pd_{70}Pt_{30}$ modified graphite electrode via a previously optimized protocol,[10b,d,e] comprising a 1 h adsorption of the enzyme on the modified graphite followed by coating of the working surface with a thin gelatin layer containing dissolved enzyme.

Figure 5 shows the glucose calibration graph obtained at a constant potential of 0 mV upon successive additions of a glucose stock solution. Regression analysis assuming a Michaelis−Menten type behavior results in a maximum current I_{max} = 54.1 μA and an apparent Micaelis constant of K_M^{app} = 45 μM.

CONCLUSIONS

A procedure for electrochemical deposition of Pd together with either Pt or Au on spectroscopic graphite was elaborated. The

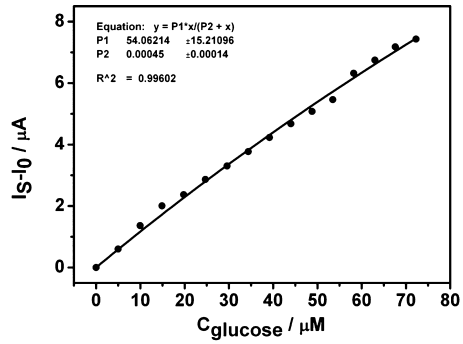

Figure 5. Background subtracted current as a function of glucose concentration (glucose oxidase/$Pd_{70}Pt_{30}$/graphite). Working potential 0 V (vs. Ag/AgCl/3 M KCl), 0.1 M phosphate buffer, pH 7.0.

presence of the second noble metal in the codeposits was found to affect both the catalytic activity and surface morphology of the codeposits. Voltammetric and SECM studies demonstrate that codeposition of Pd with either Pt or Au enhances the electrocatalytic activity for both O_2 and H_2O_2 reduction. A graphite modified with $Pd_{70}Pt_{30}$ codeposit was chosen as the basis for a H_2O_2 sensor exhibiting a sensitivity of 102 nA μM^{-1} and a linear dynamic range of up to 500 μM at an applied potential of 0 mV which is the optimal potential for the development of interference-free oxidase-based biosensors. The principle feasibility to use Pd−Pt or Pd−Au codeposits as the basis for oxidase-based biosensors was successfully demonstrated.

ASSOCIATED CONTENT

Supporting Information

Schematic representation of the droplet cell for local codeposition, SEM images of the codeposits, EDX analysis, XRD analysis, surface morphology obtained by AFM images, electrochemical characterization, SECM images, and line scans. This material is available free of charge via the Internet at http://pubs.acs.org.

AUTHOR INFORMATION

Corresponding Author

*E-mail: nina.dimcheva@uni-plovdiv.net (N.D.); wolfgang.schuhmann@rub.de (W.S.). Tel.: +49 (234)-32-26200. Fax: +49 (234)-32-14683.

Present Address

[#]Department of Chemistry, Indian Institute of Technology Ropar, Rupnagar, Punjab, India.

Notes

The authors declare no competing financial interest.

ACKNOWLEDGMENTS

The authors are grateful to the EU and the state of North Rhine-Westphalia for financial support in the framework of the Hightech.NRW project Centre of Electrochemistry − CES. N.D. acknowledges the support from the Bulgarian National Science Fund (Grant DVU 02/38).

REFERENCES

(1) Zhang, J., Ed. *PEM fuel cells electrocatalyst and catalyst layers: Fundamentals and applications*; Springer: London, 2008.

(2) You, J.-M.; Jeong, Y. N.; Ahmed, M. S.; Kim, S. K.; Choi, H. C.; Jeon, S. S. *Biosens. Bioelectron.* **2011**, *26*, 2287−2291.

(3) Chakraborty, S.; Retna Raj, C. *Biosens. Bioelectron.* **2009**, *24*, 3264−3268.
(4) Alcaide, F.; Alvarez, G.; Cabot, P. L.; Miguel, O.; Querejeta, A. *Int. J. Hydrogen Energy* **2010**, *35*, 11634−11641.
(5) Alcaide, F.; Alvarez, G.; Cabot, P. L.; Grande, H.-J.; Miguel, O.; Querejeta, A. *Int. J. Hydrogen Energy* **2011**, *36*, 4432−4439.
(6) Shi, L.; Goldbach, A.; Zeng, G.; Xu, H. *Catal. Today* **2010**, *156*, 118−123.
(7) Wang, Y.; Hernandez, R. M.; Bartlett, D. J.; Bingham, J. M., Jr.; Kline, T. R.; Sen, A.; Mallouk, T. E. *Langmuir* **2006**, *22*, 10451−10456.
(8) Gorton, L. *Anal. Chim. Acta* **1985**, *178*, 247−253.
(9) Gorton, L.; Svensson, T. *J. Mol. Catal.* **1986**, *38*, 49−60.
(10) (a) Horozova, E.; Dimcheva, N.; Jordanova, Z. *Z. Naturforsch.* **2000**, *55C*, 60−65. (b) Dimcheva, N.; Horozova, E.; Jordanova, Z. *Z. Naturforsch.* **2002**, *57C*, 705−711. (c) Dimcheva, N.; Horozova, E.; Jordanova, Z. *Z. Naturforsch.* **2002**, *57C*, 883−889. (d) Dodevska, T.; Horozova, E.; Dimcheva, N. *Anal. Bioanal. Chem.* **2006**, *386*, 1413−1418. (e) Horozova, E.; Dodevska, T.; Dimcheva, N. *Bioelectrochemistry* **2009**, *74*, 260−264. (f) Dodevska, T.; Horozova, E.; Dimcheva, N. *Cent. Eur. J. Chem.* **2010**, *8*, 19−27.
(11) Horozova, E.; Dodevska, T.; Dimcheva, N.; Mussarlieva, R. *Int. J. Electrochem.* **2011**, DOI: 10.4061/2011/697698.
(12) (a) Fernandez, J. L.; Bard, A. J. *Anal. Chem.* **2003**, *75*, 2967−2974. (b) Fernandez, J. L.; Mano, N.; Heller, A.; Bard, A. J. *Angew. Chem., Int. Ed.* **2004**, *43*, 6355−6357. (c) Fernandez, J. L.; Walsh, D. A.; Bard, A. J. *J. Am. Chem. Soc.* **2005**, *127*, 357−365. (d) Fernandez, J. L.; Raghuveer, V.; Manthiram, A.; Bard, A. J. *J. Am. Chem. Soc.* **2005**, *127*, 13100−13101.
(13) (a) Eckhard, K.; Chen, X.; Turcu, F.; Schuhmann, W. *Phys. Chem. Chem. Phys.* **2006**, *8*, 5359−5368. (b) Eckhard, K.; Etienne, M.; Schulte, A.; Schuhmann, W. *Electrochem. Commun.* **2007**, *9*, 1793−1797. (c) Maljusch, A.; Nagaiah, T. C.; Schwamborn, S.; Bron, M.; Schuhmann, W. *Anal. Chem.* **2010**, *82*, 1890−1896.
(14) Hassel, A. W.; Fushimi, K.; Seo, M. *Electrochem. Commun.* **1999**, *1*, 180−183.
(15) Chikka Nagaiah, T.; Maljusch, A.; Chen, X.; Bron, M.; Schuhmann, W. *ChemPhysChem* **2009**, *10*, 2711−2718.
(16) Kranz, C.; Ludwig, M.; Gaub, H. E.; Schuhmann, W. *Adv. Mater.* **1995**, *7*, 38−40.
(17) (a) Okunola, A. O.; Nagaiah, T. C.; Chen, X.; Eckhard, K.; Schuhmann, W.; Bron, M. *Electrochim. Acta* **2009**, *54*, 4971−4978. (b) Kundu, S.; Chikka Nagaiah, T.; Xia, W.; Wang, Y.; Van Dommele, S.; Hendrik Bitter, J.; Santa, M.; Grundmeier, G.; Bron, M.; Schuhmann, W.; Muhler, M. *J. Phys. Chem. C* **2009**, *113*, 14302−14310.
(18) Neugebauer, S.; Muller, U.; Lohmuller, T.; Spatz, J. P.; Stetzle, M.; Schuhmann, W. *Electroanalysis* **2006**, *18*, 1929−1936.
(19) (a) Kobayashi, H.; Yamauchi, M.; Kitagawa, H.; Kubota, Y.; Kato, K.; Takata, M. *J. Am. Chem. Soc.* **2010**, *132*, 5576−5577. (b) Cordero-Borboa, A. E.; Sterling-Black, E.; Gomez-Cortes, A.; Vazquez-Zavala, A. *Appl. Surf. Sci.* **2003**, *220*, 169−174. (c) Teng, X.; Wang, Q.; Liu, P.; Han, W.; Frenkel, A. I.; Wen, W.; Marinkovic, N.; Hanson, J. C.; Rodriguez, J. A. *J. Am. Chem. Soc.* **2008**, *130*, 1093−1101.
(20) (a) Scherrer, P. *Nachr. Ges. Wiss. Göttingen* **1918**, *2*, 98−100. (b) Klug, H. P.; Alexander, L. E. *X-ray Diffraction Procedures for Polycrystalline and Amorphous Materials*, 2nd ed.; John Wiley & Sons: New York, 1974.